



**AFRL-OSR-VA-TR-2013-0529**

**EXPERIMENTAL AND COMPUTATIONAL ANALYSIS OF  
INTERMITTENT FLAPPING FLIGHT**

**SCOTT THOMSON**

**BRIGHAM YOUNG UNIVERSITY**

**10/03/2013  
Final Report**

**DISTRIBUTION A: Distribution approved for public release.**

**AIR FORCE RESEARCH LABORATORY  
AF OFFICE OF SCIENTIFIC RESEARCH (AFOSR)/RSA  
ARLINGTON, VIRGINIA 22203  
AIR FORCE MATERIEL COMMAND**

<b>REPORT DOCUMENTATION PAGE</b>				<i>Form Approved</i> <b>OMB No. 0704-0188</b>	
Public reporting burden for this collection of information is estimated to average 1 hour per response, including the time for reviewing instructions, searching existing data sources, gathering and maintaining the data needed, and completing and reviewing this collection of information. Send comments regarding this burden estimate or any other aspect of this collection of information, including suggestions for reducing this burden to Department of Defense, Washington Headquarters Services, Directorate for Information Operations and Reports (0704-0188), 1215 Jefferson Davis Highway, Suite 1204, Arlington, VA 22202-4302. Respondents should be aware that notwithstanding any other provision of law, no person shall be subject to any penalty for failing to comply with a collection of information if it does not display a currently valid OMB control number. <b>PLEASE DO NOT RETURN YOUR FORM TO THE ABOVE ADDRESS.</b>					
<b>1. REPORT DATE (DD-MM-YYYY)</b> 02-10-2013		<b>2. REPORT TYPE</b> Final Report		<b>3. DATES COVERED (From - To)</b> July 1, 2010 to June 30, 2013	
<b>4. TITLE AND SUBTITLE</b> Experimental and Computational Analysis of Intermittent Flapping Flight				<b>5a. CONTRACT NUMBER</b>	
				<b>5b. GRANT NUMBER</b> FA9550-10-1-0334	
				<b>5c. PROGRAM ELEMENT NUMBER</b>	
<b>6. AUTHOR(S)</b> Thomson, Scott, L. Colton, Mark, B. Mattson, Christopher, A. Truscott, Tadd, T.				<b>5d. PROJECT NUMBER</b>	
				<b>5e. TASK NUMBER</b>	
				<b>5f. WORK UNIT NUMBER</b>	
<b>7. PERFORMING ORGANIZATION NAME(S) AND ADDRESS(ES)</b> Brigham Young University Office of Research & Creative Activities University Hill Provo, UT 84602-1231				<b>8. PERFORMING ORGANIZATION REPORT NUMBER</b> None.	
<b>9. SPONSORING / MONITORING AGENCY NAME(S) AND ADDRESS(ES)</b> USAF, AFRL AF Office of Scientific Research 875 N Randolph Street, Rm 3112 Arlington, VA 22203 PM: Dr. Douglas Smith				<b>10. SPONSOR/MONITOR'S ACRONYM(S)</b> AFOSR	
				<b>11. SPONSOR/MONITOR'S REPORT NUMBER(S)</b> None	
<b>12. DISTRIBUTION / AVAILABILITY STATEMENT</b> Distribution A: Approved for Public Release, Distribution is Unlimited.					
<b>13. SUPPLEMENTARY NOTES</b> None					
<b>14. ABSTRACT</b> The purpose of the research performed under this grant was to explore aerodynamics and flow-solid interactions of a flapping wing mechanism. This was accomplished by performing research in the following four areas: 1. Development and testing of a flapping mechanism featuring adjustable wing kinematics. 2. Exploration of different kinematic representations of flapping wing trajectories. 3. Study of hardware-in-the-loop optimization approaches. 4. Full-field, high-speed, three-dimensional flow imaging using synthetic aperture particle image velocimetry (SAPIV). The outcomes of these activities are summarized in the report. Where not available in publications or theses, methodological details are provided. It is shown that SAPIV is able to reconstruct 3D whole-field velocity fields in large spatial regions of interest. The results demonstrate that SAPIV can be used to measure fluid flow velocities and reconstruct the visual hull of flapping wings, benefiting future work in studying the complex and unsteady nature of flapping flight.					
<b>15. SUBJECT TERMS</b> Flapping flight, wing kinematics, hardware-in-the-loop optimization, synthetic aperture particle image velocimetry (SAPIV)					
<b>16. SECURITY CLASSIFICATION OF:</b>			<b>17. LIMITATION OF ABSTRACT</b> UU	<b>18. NUMBER OF PAGES</b>	<b>19a. NAME OF RESPONSIBLE PERSON</b> Scott Thomson
<b>a. REPORT</b> U	<b>b. ABSTRACT</b> U	<b>c. THIS PAGE</b> U			<b>19b. TELEPHONE NUMBER (include area code)</b> 801-422-4980

Final Report for AFOSR Grant Number FA9550-10-1-0334  
for the period July 1, 2010, to June 30, 2013

**Experimental and Computational Analysis of Intermittent Flapping Flight**

Scott L. Thomson (801-422-4980, thomson@byu.edu)  
Mark B. Colton (801-422-6303, colton@byu.edu)  
Christopher A. Mattson (801-422-6544, mattson@byu.edu)  
Tadd T. Truscott (801-422-6545, truscott@byu.edu)  
Department of Mechanical Engineering  
Brigham Young University  
435 CTB  
Provo, UT 84602

**1. INTRODUCTION AND PROBLEM STATEMENT**

Micro air vehicles (MAVs) – vehicles with a maximum dimension of no more than 15 cm – offer attractive solutions for applications such as surveillance, reconnaissance, and search and rescue operations. The reduction in size is accompanied by a change in aerodynamic flight regime, characterized by a relatively low Reynolds number. In this regime, flapping flight introduces several aerodynamic advantages, as evidenced by the ubiquitous use of flapping flight by various animals (for example, about 75% of the approximately 13,000 species of warm-blooded vertebrates fly).

Many aspects of flapping flight aerodynamics, however, are yet to be fully understood, such as unsteady aerodynamic lift-enhancing phenomena, identification and characterization of flow separation and reattachment physics, laminar-to-turbulent transition, and transient vortex dynamics. Animal flight in nature is replete with a wide variety of features, the physics and benefits of which are also not yet fully understood, such as compliant and adjustable wings, widely varying flapping wing kinematics, and extreme maneuverability.

The purpose of the research performed under this grant was to explore aerodynamics and flow-solid interactions of a flapping wing mechanism. This was accomplished by performing research in the following four areas:

1. Development and testing of a flapping mechanism featuring adjustable wing kinematics.
2. Exploration of different kinematic representations of flapping wing trajectories.
3. Study of hardware-in-the-loop optimization approaches.
4. Three-dimensional flow imaging using synthetic aperture particle image velocimetry (SAPIV).

The outcomes of these four activities are summarized below.

**2. DEVELOPMENT AND TESTING OF FLAPPING MECHANISM WITH ADJUSTABLE KINEMATICS**

A robotic flapping wing mechanism for use in general studies involving flapping flight and laboratory-based experimental optimization of flapping trajectories was designed and fabricated (see Fig. 1). The design allows for dynamic adjustment of flapping trajectories in air or liquids with three rotational degrees of freedom on each wing. The mechanism design has adjustable kinematics, can operate in water, oil, or air, is fixed, and can be used for flow visualization, particle image velocimetry (PIV), and force analysis. The mechanism is described in detail in [1,2]. The mechanism was used in a custom-built tank (see Fig. 2 and Ref. [3]).

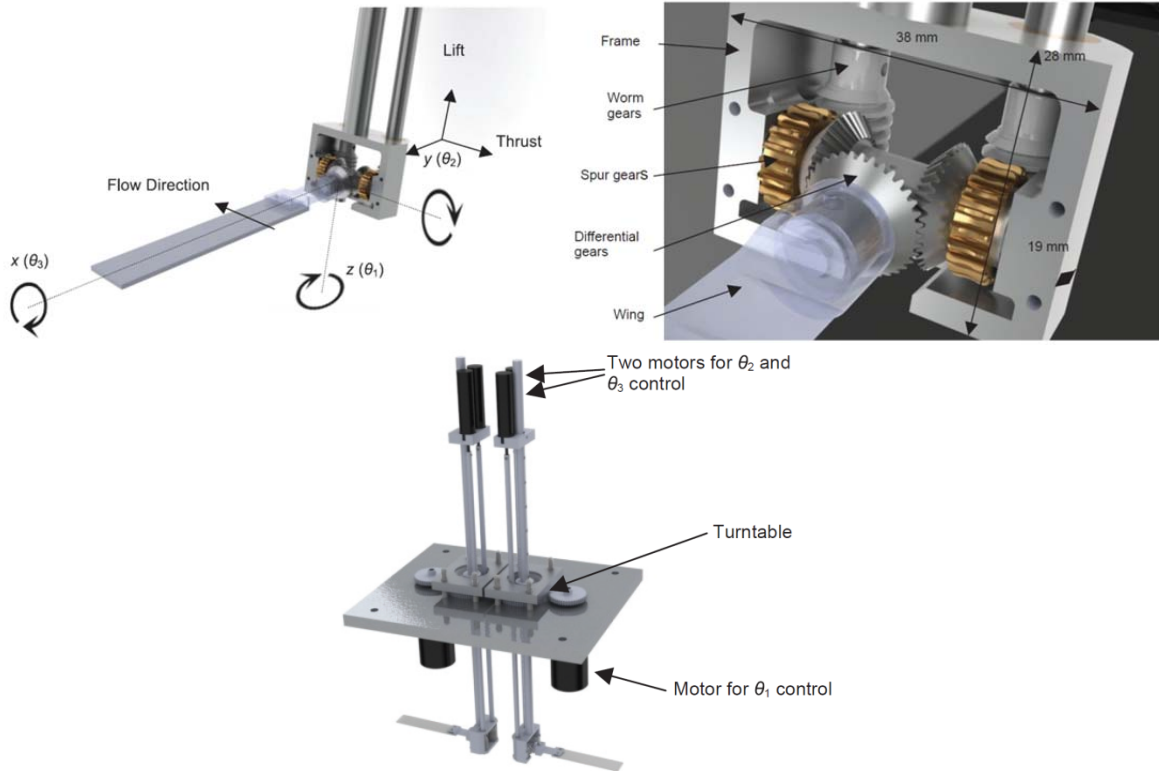


**Figure 1.** Renderings of flapping mechanism.

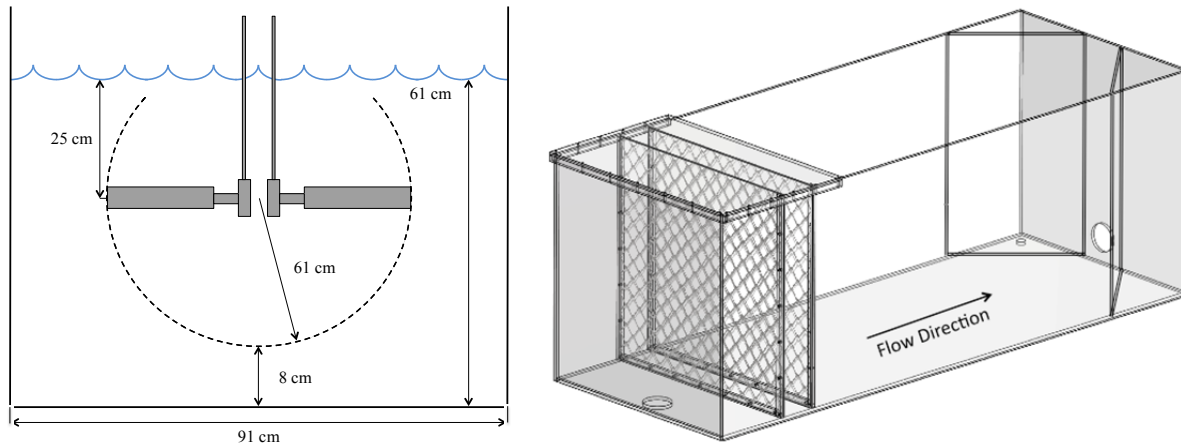


**Figure 2.** Flow tank schematics. Left: Cross-section showing submerged mechanism. Right: Tank only.

### 3. THEORETICAL COMPARISON OF WING TRAJECTORY KINEMATICS

In the work described in [1,2], the parameters of a simple Fourier series representation of the wing angles were optimized using a hardware-in-the-loop approach. The follow-on study summarized here investigated the use of other kinematic representations. The objective was to explore the relative strengths of the candidate representations, refine the optimization methods, and implement the most promising in hardware-in-the-loop optimization to find the best parameters. A novel kinematic representation was developed to enable modulation of the down-stroke-to-up-stroke ratio of a flapping cycle. Details will appear in [4], but are here included because they are not yet widely available.

### 3.1 Wing Trajectories

An initial study was directed at narrowing the pool of candidate kinematic representations through simulation. Kinematic schemes were sought that were capable of representing the most general flapping patterns, including those with a biological basis, with the fewest kinematic parameters. Candidate representations included standard sinusoids, polar and Cartesian Fourier series, piecewise linear segments, piecewise-defined sinusoids, NURBS, and scaled sinusoids.

Based on the initial simulation studies, the polar Fourier series and the scaled sinusoids from Berman and Wang (2007) were selected for further study. Using the Fourier series, the wing angles are defined by

$$\begin{aligned}\theta_s(t') &= A_{0,S} + \sum_{n=1}^{\infty} A_{n,S} \sin[2\pi n t' - \phi_{n,S}] \\ \theta_p(t') &= A_{0,P} + \sum_{n=1}^{\infty} A_{n,P} \cos[2\pi n t' - \phi_{n,P}] \\ \theta_d(t') &= A_{0,D} + \sum_{n=1}^{\infty} A_{n,D} \cos[2\pi n t' - \phi_{n,D}]\end{aligned}$$

where  $\theta_s$  is the sweep angle,  $\theta_p$  is the pitch angle, and  $\theta_d$  is the deviation angle of the wing;  $A_n$  are the kinematic coefficients;  $\phi_n$  are the phase delay parameters; and  $t'$  is the nondimensionalized time given by

$$t' = t/T = ft$$

where  $f$  is the flapping frequency,  $T$  is the period, and  $t$  is the time. The 11 parameters of the polar Fourier method to be found through hardware-in-the-loop optimization are shown in Table 1.

**Table 1.** Polar Fourier Kinematic Parameters

Input Parameters	Symbol
Stroke Plane Angle	$\Psi$
<b>Sweep:</b>	
Amplitude of First Frequency	$A_{1,S}$
<b>Pitch:</b>	
Constant Pitch Offset	$A_{0,P}$
Amplitude of First Frequency	$A_{1,P}$
Phase Delay of First Frequency	$\phi_{1,P}$
Amplitude of Second Frequency	$A_{2,P}$
Phase Delay of Second Frequency	$\phi_{2,P}$
<b>Deviation:</b>	
Constant Pitch Offset	$A_{0,D}$
Amplitude of First Frequency	$A_{1,D}$
Amplitude of Second Frequency	$A_{2,D}$
Phase Delay of Second Frequency	$\phi_{2,D}$

A novel kinematic method was developed, based on the pitch and sweep representation employed by Berman and Wang (2007), with two key features:

1. *A non-sinusoidal form of the periodic function.* The work resulted in the unification of the Berman and Wang equations through coordinate transformations to enable continuous variation of the shape from triangular to square with the variation of a single parameter.
2. *A novel method of modifying the down-stroke-to-up-stroke ratio with a single parameter.* This is done without sacrificing the continuity of the function or its first three derivatives. This enables the robotic mechanism to execute trajectories with unequal half-stroke durations.

In the Modified Berman and Wang method the wing angle trajectories are calculated using

$$\begin{aligned}\theta_s(t') &= A_{0,S} + \sum_{n=1}^{\infty} A_{n,S} \Theta_{\sin}(t', \phi_{n,S}, K_{n,S})_n \\ \theta_p(t') &= A_{0,P} + \sum_{n=1}^{\infty} A_{n,P} \Theta_{\cos}(t', \phi_{n,P}, K_{n,P})_n \\ \theta_d(t') &= A_{0,D} + \sum_{n=1}^{\infty} A_{n,D} \Theta_{\cos}(t', \phi_{n,D}, K_{n,D})_n\end{aligned}$$

Here,  $\Theta_{\sin}(t', \phi_{n,m}, K_{n,m})_n$  and  $\Theta_{\cos}(t', \phi_{n,m}, K_{n,m})_n$  are given by

$$\begin{aligned}\Theta_{\sin}(t', \phi_{n,m}, K_{n,m})_n &= \begin{cases} \frac{\sin^{-1}[K_{n,m} \sin(2\pi n\tau(t') - \phi_{n,m})]}{\sin^{-1} K_{n,m}} & \alpha_{m,n} < 0 \\ & \text{(Triangular)} \\ \sin(2\pi n\tau(t') - \phi_{n,m}) & \alpha_{m,n} \cong 0 \\ & \text{(Sinusoidal)} \\ \frac{\tanh[K_{n,m} \sin(2\pi n\tau(t') - \phi_{n,m})]}{\tanh K_{n,m}} & \alpha_{m,n} > 0 \\ & \text{(Square)} \end{cases} \\ \Theta_{\cos}(t', \phi_{n,m}, K_{n,m})_n &= \begin{cases} \frac{\sin^{-1}[K_{n,m} \cos(2\pi n\tau(t') - \phi_{n,m})]}{\sin^{-1} K_{n,m}} & \alpha_{m,n} < 0 \\ & \text{(Triangular)} \\ \cos(2\pi n\tau(t') - \phi_{n,m}) & \alpha_{m,n} \cong 0 \\ & \text{(Sinusoidal)} \\ \frac{\tanh[K_{n,m} \cos(2\pi n\tau(t') - \phi_{n,m})]}{\tanh K_{n,m}} & \alpha_{m,n} > 0 \\ & \text{(Square)} \end{cases}\end{aligned}$$

The relationship between  $\alpha_{n,m}$  and  $K_{n,m}$  is given by

$$K = \begin{cases} 1 - 10^{\alpha/100} & -\infty < \alpha < 0, \quad (\text{Triangular}) \\ 0 & \alpha \cong 0, \quad (\text{Sinusoidal}) \\ 10^{\alpha/100} - 1 & 0 < \alpha < \infty, \quad (\text{Square}). \end{cases}$$

Additionally, the function  $\tau(t')$  is a “pseudo-time” function that enables variation of the down-stroke-to-up-stroke ratio. The subscript  $m$  designates either sweep ( $s$ ), pitch ( $p$ ), or deviation from the stroke plane ( $d$ ). The 17 parameters of the Modified Berman and Wang method to be found through hardware-in-the-loop optimization are shown in Table 2.

**Table 1:** Inputs for Modified Berman and Wang Kinematics

Input Parameters	Symbol
Stroke Plane Angle	$\Psi$
Down-stroke-to-Up-stroke Ratio	$DU_{ratio}$
<b>Sweep:</b>	
Amplitude of First Frequency	$A_{1,S}$
Shape of First Frequency	$\alpha_{1,S}$
<b>Pitch:</b>	
Constant Pitch Offset	$A_{0,P}$
Amplitude of First Frequency	$A_{1,P}$
Phase Delay of First Frequency	$\phi_{1,P}$
Shape of First Frequency	$\alpha_{1,P}$
Amplitude of Second Frequency	$A_{2,P}$
Phase Delay of Second Frequency	$\phi_{2,P}$
Shape of Second Frequency	$\alpha_{2,P}$
<b>Deviation:</b>	
Constant Pitch Offset	$A_{0,D}$
Amplitude of First Frequency	$A_{1,D}$
Shape of First Frequency	$\alpha_{1,D}$
Amplitude of Second Frequency	$A_{2,D}$
Phase Delay of Second Frequency	$\phi_{2,D}$
Shape of Second Frequency	$\alpha_{2,D}$

### 3.2 Experimental Approach

The two kinematic representations described above were used in hardware-in-the-loop experiments to determine the optimal parameters (Table 1 and Table 2), and therefore the optimal trajectory, to maximize lift. Note that other cost functions could be explored that will optimize thrust, lift/thrust combinations, efficiency, or other flight parameters. The optimization method is similar to a Box-Behnken/Response Surface method, but with modifications that include intelligent step size selection, exclusion of insignificant parameters from the kinematic models, and termination criteria.

The same hardware was used, with the exception that a new shear force sensor was incorporated into the wing, allowing a more accurate measurement of wing forces. The wing angles were defined

using the sweep, pitch, and deviation angles described above, and converted into joint angles using a series of coordinate transformations. Tracking of each joint was achieved with decoupled PID loops implemented in National Instruments real-time hardware.

### 3.3 Optimization Results

Initial conditions were assigned for each of the kinematic representations and the modified Box-Behnken optimization routine was used to cover the parameter space and determine the kinematic parameters that optimize lift on the robotic flapping mechanism. The evolution of the optimization for both kinematic representations is shown in Fig. 3. Figure 3a shows a plot of lift vs. thrust for each iteration of the optimization process. As can be seen from the figure, as the hardware-in-the-loop optimization proceeded, trajectories were found that resulted in improved lift for both representations. Figure 3b shows the evolution of the fitness (cost) function as the optimization proceeds, illustrating that the method results in decreasing values of the fitness function, implying that the each iteration improves over the previous.

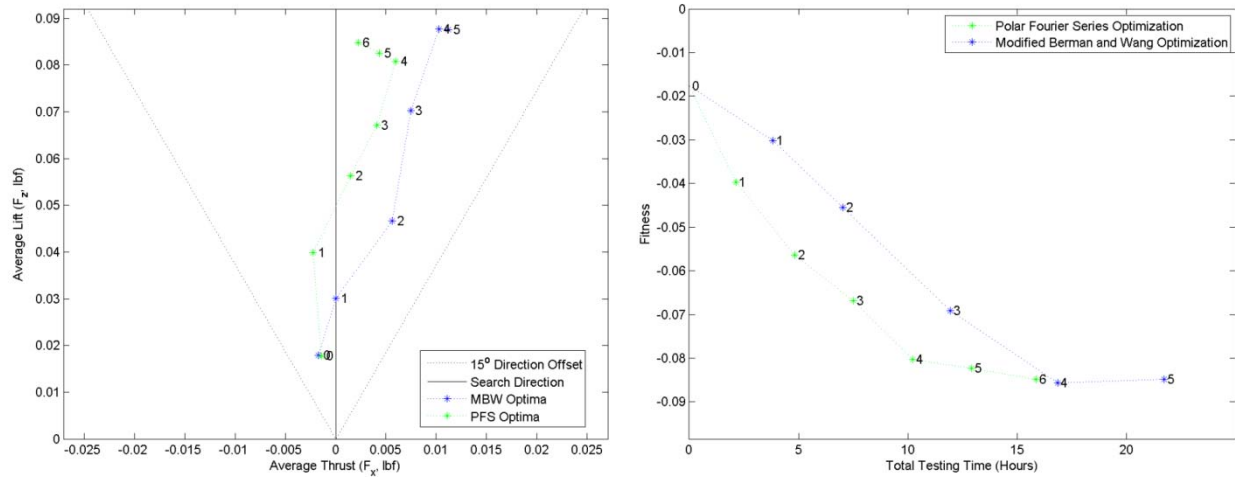


**Figure 3.** Evolution of lift and thrust (left) and fitness function (right) for successive optimization iterations.

The evolution of the kinematic parameters is shown in Table 3 (polar Fourier series) and Table 4 (Modified Berman and Wang). The tables are color coded to highlight those regions where significant change is going on. For the polar Fourier series (Table 3), the most significant changes are observed for the amplitude of the sweep angle ( $A_{1,S}$ ) and the amplitude of the second deviation angle harmonic ( $A_{2,D}$ ).

**Table 3.** Center Point Changes, Polar Fourier Series

	$\Psi$	$A_{1,S}$	$A_{0,P}$	$A_{1,P}$	$\phi_{1,P}$	$A_{2,P}$	$\phi_{2,P}$	$A_{0,D}$	$A_{1,D}$	$A_{2,D}$	$\phi_{2,D}$
<b>Iteration 2</b>	-1.01	15	0.80	-9.24	-3.95	0.50	0	2.96	-1.50	-9.32	0
<b>Iteration 3</b>	0	8.56	0	0	0	0	0	0	-7.98	-8.42	15
<b>Iteration 4</b>	0	6.27	0	0	0	0	0	0	3.82	-4.00	0
<b>Iteration 5</b>	0	4.64	0	0	0	0	0	0	4.38	-4.72	-15
<b>Iteration 6</b>	0.56	3.40	-3.58	-4.52	7.39	5.46	0	3.34	-0.70	-3.67	5.43
<b>Optimum</b>	0.23	0.96	-1.37	-0.99	0.45	4.48	9.70	0.39	0.57	-0.64	2.28



**Table 2.** Center Point Changes, Modified Berman and Wang

	$\Psi$	$DU_{ratio}$	$A_{1,S}$	$\alpha_{1,S}$	$A_{0,P}$	$A_{1,P}$	$\phi_{1,P}$	$\alpha_{1,P}$	$A_{2,P}$	$\phi_{2,P}$	$\alpha_{2,P}$	$A_{0,D}$	$A_{1,D}$	$\alpha_{1,D}$	$A_{2,D}$	$\phi_{2,D}$	$\alpha_{2,D}$
<b>Iteration 2</b>	0	20	12.57	0	0	-7.39	0	-30	0	0	0	0	0	0	0	0	0
<b>Iteration 3</b>	-0.71	-7.73	9.32	8.19	-1.40	-9.17	-0.62	13.39	1.15	0	0	3.70	-0.88	0	-6.74	0	0
<b>Iteration 4</b>	0	0	13.65	0	0	0	0	0	0	0	0	0	0	0	-15	0	0
<b>Iteration 5</b>	0	0	6.41	0	0	0	0	0	0	0	0	0	0	0	-9.46	0	0
<b>Optimum</b>	0.79	-1.11	0.20	-0.65	-0.99	1.13	1.73	10.66	1.54	0	0	-4.12	-0.38	0	-4.70	0.59	0

For the Modified Berman and Wang method (Table 4), it becomes evident here that certain parameters begin the optimization routine with large step sizes which are reduced for later iterations. Again, the primary example of this is the sweep amplitude ( $A_{1,S}$ ). These parameters tend to dominate the effect on the fitness function early on, but that influence is reduced as the wing motion approaches the limits of the joint angles.

Other observations can be made from this data as well. For instance, there are variables unique to the Modified Berman and Wang trajectory generator which are not used at all during the test ( $\alpha_{2,P}$ ,  $\alpha_{1,D}$ ,  $\alpha_{2,D}$ ). Of the parameters unique to Modified Berman and Wang, three moved through the design space. The first of these, the down-stroke-to-up-stroke ratio modifier ( $DU_{ratio}$ ), was raised by 20%, the full value allowed during the first iteration. In the second iteration it returned back toward its origin, ending at 12.27%. During the final iteration, it adjusted downward slightly to finish at 11.15%. This means that for the initial portion of the optimization routine, benefit was derived by lengthening the duration of the down-stroke, while later in the process, benefit was had by equalizing the durations of the two half strokes. The other active parameters were the shape of the sweep and pitch fundamental frequencies ( $\alpha_{1,S}$  and  $\alpha_{1,P}$ ).

Parameters not unique to Modified Berman and Wang were also fairly inactive throughout the process. Table 2 shows that these included the pitch offset ( $A_{0,P}$ ), the phase shift of the first pitch harmonic ( $\phi_{1,P}$ ), the second amplitude in pitch ( $A_{2,P}$ ), and the second phase shift in pitch ( $\phi_{2,P}$ ) among others. Additionally, the stroke plane angle  $\Psi$  stayed fairly constant throughout the process.

#### 4. EFFICIENT HARDWARE-IN-THE-LOOP OPTIMIZATION

Hardware-in-the-loop (HIL) modeling is the use of physical hardware to represent a system (as opposed to an analytical or computational model). One advantage of HIL modeling is that it can avoid problems caused by inaccurate models. Complicated phenomena may be difficult to model accurately, but they can act on a hardware model similarly to how they would act on a real system. Another benefit of HIL modeling is manifest when accurate models cannot be obtained because of time or other constraints. In cases like these, a system can be modeled by a HIL model, which is treated as a black box that returns performance outputs given inputs.

Some researchers have used HIL in the study of flapping flight. However, HIL has some challenges when used in optimization. Sometimes, HIL models are too expensive to call exhaustively. The HIL system used previously [1,2] has a large, complex design space and sampling the whole space with a central composite design of experiments could require over 32,000 calls. While this test would take a long time to complete, it would also result in system wear. In cases like this, mechanical wear can contaminate the results of the test. This makes the hardware too expensive to use in a normal optimization algorithm. Instead, a less expensive model is needed for optimization. In this research, the use of a physics-based model as a surrogate was studied as a means for reducing the number of hardware calls while maintaining the benefits of HIL modeling. The below is a summary of the methods and results presented in [5,6].

#### 4.1 Approach

An approach to variable fidelity, hardware-in-the-loop optimization that minimizes calls to the hardware is here presented. The basis of this approach is an intelligent DOE (IDOE) that is informed by physics. As such, the intent of this research was to create an IDOE. An IDOE chooses points to test that are predicted to have better objectives than the previous points. This requires something that can provide accurate information about the hardware without actually calling the hardware. A physics-based surrogate model can fill this role. The physics-based model predicts optimal solutions and gives information about how different design variables affect the performance of the hardware. This information can be used to choose the next point or points for the DOE to test.

#### 4.2 Intelligent DOE

In order to take advantage of the similarities between a physics-based model and a hardware model, some mapping between the expensive hardware model and the inexpensive physics model must be made. This mapping allows the physics model to provide useful information about the hardware model by relating points within the physics model space to corresponding ones in the hardware model space. In order to create this mapping, some assumptions must be made about the differences between the models. In this research, the assumption was that a point in the hardware model space,  $x_h$ , can be represented as a point in the physics model with some shift,  $\gamma$ . Also, the objective values may differ by some scaling factor  $\alpha$ . The two models, then, can be related by the expression  $H(x_h) = \alpha P(x_p - \gamma)$ , where  $x_p$  is a point within the physics model space and  $x_h$  is a point within the hardware model design space.  $H$  represents the hardware model and  $P$  represents the physics model. Since  $x_p$  is an element within the design space and  $\gamma$  is defined within the same space, both are vectors of the same number of dimensions as the physics model has. There are other potential differences between the models, such as stretching; however, for many situations, the differences discussed here are sufficient to map the models sufficiently well for optimization purposes.

#### 4.3 Algorithm

Here, the steps in the intelligent DOE are outlined. The optimization problem can be stated as

$$\min_x H(x)$$

subject to

$$\text{linear constraints} \leq 0$$

$$\text{nonlinear constraints} \leq 0$$

where  $H(x)$  is the hardware model.

The next step to finding the hardware model solution,  $x_h^*$ , is to find values for  $\alpha$  and  $\gamma$  for which  $H(x_p^*) = \alpha P(x_{p,i}^* - \gamma)$ , where  $x_p^* = x_{p,i}^* - \gamma$ , and  $x_{p,i}^*$  is the initial optimal solution of the physics model. When these values have been found,  $x_h^* = x_p^*$ .

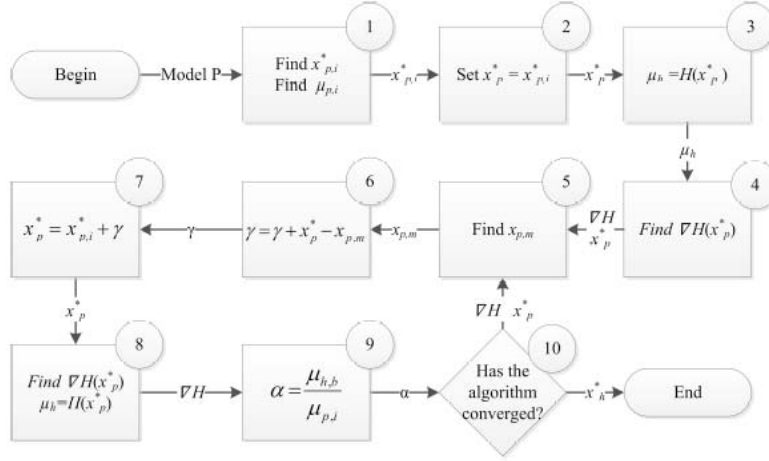


**Figure 4.** Flowchart of the intelligent DOE

Figure 4 shows a flowchart of the entire method. First, the user finds the optimal solution,  $x_{p,i}^*$ , to the low cost physics model. This involves setting bounds on the space, choosing a starting point, and using a known optimization technique. The optimization problem is expressed by

$$\min_{x_p} P(x_p)$$

subject to

$$\text{linear constraints} \leq 0$$

$$\text{nonlinear constraints} \leq 0$$

where  $P(x)$  is the physics model.

In this research, gradient-based algorithms were used, however, genetic or other algorithms could be effective, depending on the nature of the model.  $\mu_{p,i}$  is the objective value at  $x_{p,i}^*$ . Step 2 sets  $x_p^* = x_{p,i}^*$ .  $x_{p,i}^*$  is the initial solution to the physics model and does not change throughout the algorithm, while  $x_p^*$  does change as the physics model is shifted. Step 3 calls the hardware model,  $H$ , at the physics model solution,  $x_p^*$ , and sets the result as  $\mu_h$ . Step 4 finds the gradient of the hardware model at  $x_p^*$ . Steps 5 through 10 are repeated until the algorithm converges. Once  $\nabla H(x_p^*)$  has been found, step 5 finds the point,  $x_{p,m}$ , where the physics model gradient matches the gradient measured in the hardware. This step is an optimization problem that can be stated as

$$\min_x L(x)$$

subject to

$$\text{linear constraints} \leq 0$$

$$\text{nonlinear constraints} \leq 0.$$

Where

$$L = \|\nabla H(x_p^*) - \nabla P(x_{p,m})\|$$

This is done with known optimization techniques. Here, gradient-based and genetic algorithms were used as needed by the problem. Step 6 finds the offset between the hardware and physics models,  $\gamma$ , by subtracting  $x_{p,m}$  from  $x_p^*$ . This difference is added to the existing offset, which is initially zero, and the physics model is shifted by this amount. Next, step 7 defines the new  $x_p^*$  by shifting it by the offset so that it does not move relative to the physics model.  $\mu_h$  and  $\nabla H$  are found at this new  $x_p^*$  in step 8. Step 9 updates  $\alpha$  by dividing the best value returned by the hardware,  $\mu_{h,b}$ , by  $\mu_{p,i}$ , the value of the physics model at  $x_{p,i}^*$ . This scale must be accurate in order for the physics gradients to be correct. Finally, step 10 checks for convergence. This can be done using any appropriate criteria. A convergence criteria for variable fidelity optimization is presented in the literature, however, this uses a traditional response surface, which allows for many calls. This method can require a prohibitive number of function calls when calling the expensive physics model. Two alternative convergence criteria requiring no additional hardware calls are presented here. One criterion is whether the gradient was zero. As is the case with some gradient-based algorithms, this can terminate the algorithm at local maxima, minima, or saddle points, so care should be taken to ensure that solutions reached with these criteria are optimal. In many cases, solutions to engineering problems are constrained, which means, among other things, that the gradients are non-zero. For cases like this, convergence can be triggered when  $\nabla P(x_p^*) = \nabla H(x_h^*)$ . This criterion, in effect, is triggered when the hardware point that corresponds to the physics model solution,  $x_p^*$ , has been found. This assumes that the scale,  $\alpha$ , and the offset,  $\gamma$  have been found correctly. Other convergence criteria could be used, depending on the nature of the problem being solved. Using these steps, the physics model shifts and scales until it matches the hardware model at the solution and  $x_p^* = x_h^*$ . As can be seen in the flowchart, each time steps 5-10 are iterated, the hardware gradient must be found. Thus, the number of hardware calls needed for the IDOE to converge is directly related to the number of iterations of the algorithm and it is desirable to find the solution with as few iterations as possible.

Figure 5 shows plots of hypothetical hardware and physics models after each iteration of a one-dimensional test. The objective of this problem is to minimize the value returned by the hardware. Here, the hardware model has been scaled by a factor of  $\alpha = 1.3$  and shifted by  $\gamma = 20^\circ$ . Figure 5a shows the models in their initial state. Notice that it has larger negative value than  $\mu_{p,i}$  which is caused by the fact that the hardware model is scaled larger than the physics one. In iteration 2,  $\alpha$  and  $\gamma$  have been updated so that the physics model is nearly equal to the hardware model. By the third iteration, shown in Fig. 5c, the models are equal and the solution to the hardware model,  $x_h^*$  equals the known solution to the physics model,  $x_p^*$ .

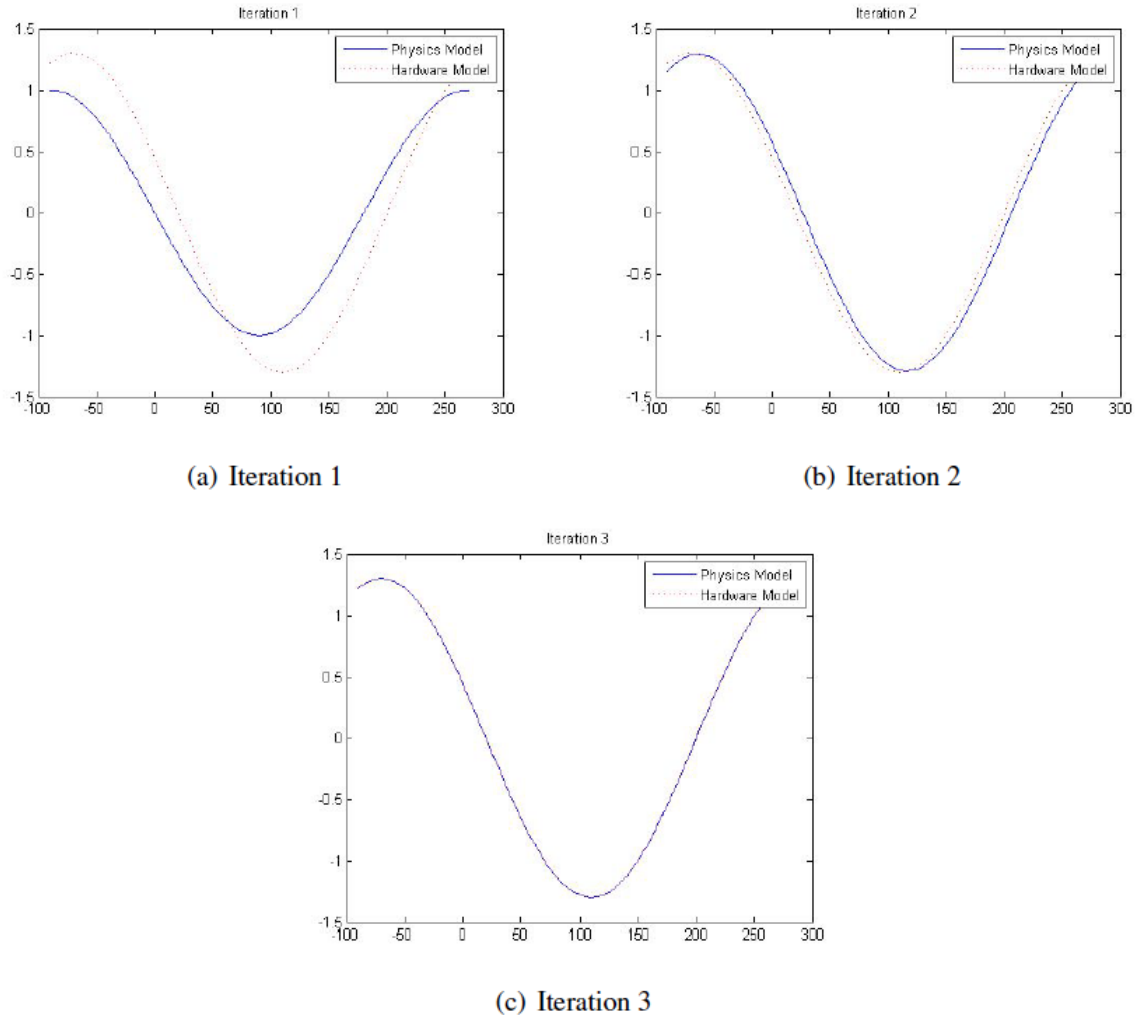


**Figure 5.** Progression of the IDOE through a sample optimization routine.

#### 4.4 Validation and Verification

After development, the intelligent DOE (IDOE) was verified on several problems of varying complexity. This allowed for testing of a variety of scenarios. Each example problem was optimized by the IDOE and two DOE-based VFO routines for comparison. The results are provided in [5].

#### 5. SYNTHETIC APERTURE PARTICLE IMAGE VELOCIMETRY

Three-dimensional velocity measurements of the flow fields around a tethered mechanical flapper were obtained using synthetic aperture PIV (SAPIV). The results focused mainly on the leading and trailing edge vortices (LEV, TEV) through an entire flapping cycle. The results were compared to velocity measurements taken using 2D PIV. Additionally, force measurements of the lift and thrust generated by the mechanical flapper were taken. The visual hull of the mechanical flapper was reconstructed. The methods and results are being prepared for a manuscript [7] (anticipated for submission Fall 2013), but are included here since they are not yet widely available.

Measurements were performed on a commercially available MAV, powered by a small electric motor that drives a pivoting mechanism at the front edge of the wings, with the back edge of the wings pinned (Fig. 6). A strut forms the leading edge of the wings with the rest of the wings made of a thin, plastic membrane. Steering is accomplished by moving the pinned back edges of the wings up or down,

depending on the direction of the turn. The mechanism is controlled via wireless remote. Stability is achieved through a fixed tail section connected to the back of the body. The wing beat frequency was 15.9 Hz, resulting in a Reynolds number (calculated using the induced forward velocity and mean chord length) of 9600 and a Strouhal number of 0.79.

The experiments were performed in a 61 x 41 x 30 cm<sup>3</sup> custom acrylic observation tank, providing complete optical access (Fig. 6). The MAV was tethered to a steel plate in the center of the tank. The synthetic aperture setup consisted of eight Photron SA3 high-speed video cameras. The cameras were equipped with 50 mm lenses and arranged in an array such that every camera was looking at the same region of interest. The camera array was positioned parallel to the long axis of the observation tank. A Darwin-Duo laser system (Quantronix, Nd:YLF, 1000 Hz) was used to provide PIV illumination. This laser uses two laser pulses at 500 Hz each, corresponding to PIV at 500 Hz. The laser was positioned perpendicular to the cameras. A beam expander from Edmunds Optics enlarged the beam to a cross sectional area of 55.8 cm<sup>2</sup>. The air inside the tank was seeded with hollow polymer microspheres with a mean diameter of 40 µm and a density of 25 kg/m<sup>3</sup> (Expancel, 461 DET 40 d25).

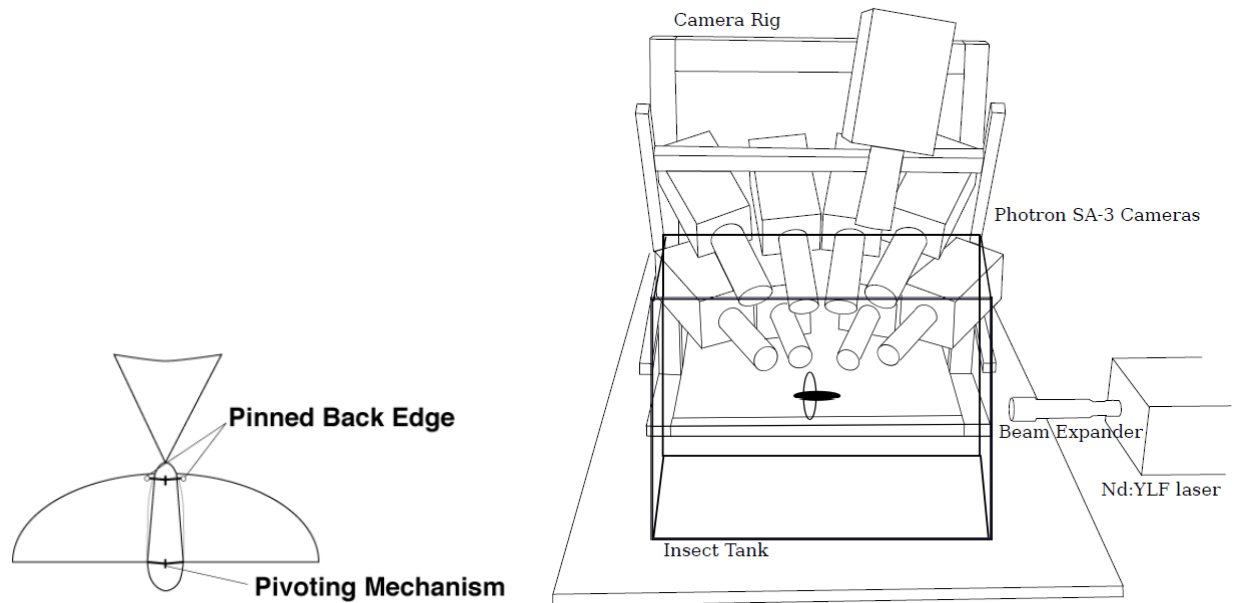


**Figure 6.** Line drawings of the MAV (left) and experimental setup (right). Eight high-speed cameras were used to perform SAPIV. A ninth camera, above the tank, could be used for wing tracking.

Three-dimensional, time-resolved fluid velocities were obtained by using 3D SAPIV. SAPIV is based on the principles of light field imaging. The essential idea is that an array of cameras can image an object from multiple viewpoints. Since each viewpoint sees the object from a different angle, the images from each camera can be digitally refocused to create a set of images that are in focus at different planes throughout the region of interest, known as a focal stack. The use of multiple viewpoints has several advantages, such as allowing for high-density seeding, because of the ability to see around partial occlusions. Particles that are in focus on a given plane will have a higher intensity than particles that are not in focus. The out-of-focus particles can be eliminated from the image planes using thresholding. The digitally refocused and thresholded image pairs can then be passed to a standard 3D PIV system such as matPIV for cross correlation (Belden et al, 2010). The cameras were calibrated using a process based on the Multi-camera Self Calibration Method developed by Svoboda et al. (2005). The preprocessed images from each of the eight cameras, and the camera projection matrix, were passed to the SAPIV software. A

map-shift-average algorithm was used to digitally refocus the images onto synthetic focal planes to create a focal stack. SAPIV code is available at [www.saimaging.org](http://www.saimaging.org).

The lift and thrust forces generated by the flapping wing of the MAV were measured with a single axis load cell. Force measurements were taken for 10 different runs, with 55 flapping periods in each run for statistical analysis. The MAV was mounted in two configurations - horizontally for lift measurements, and vertically for thrust measurements. A single SA3 camera was synchronized with the load cell to document the position of the MAV wings as force data points were acquired. The load cell sampled at 4000 Hz and the camera sampled at 2000 Hz.

Figure 7 shows the wing of the MAV through a partial (last 75%) down-stroke in the left two columns and a partial (first 75%) up-stroke in the right two columns, with vorticity plotted as iso-surfaces. The presence of an LEV and a TEV are recognized on the leading edge (left side) and trailing edge (right side) of the wing, respectively. The wing was recreated in the plots using the visual hull method. The recreated wing is not visible in the plots when the actual wing drops below the laser volume and at times when the amount of particles gives the visual hull algorithm difficulty. However, LEVs and TEVs are still visible in their respective positions in the plots.

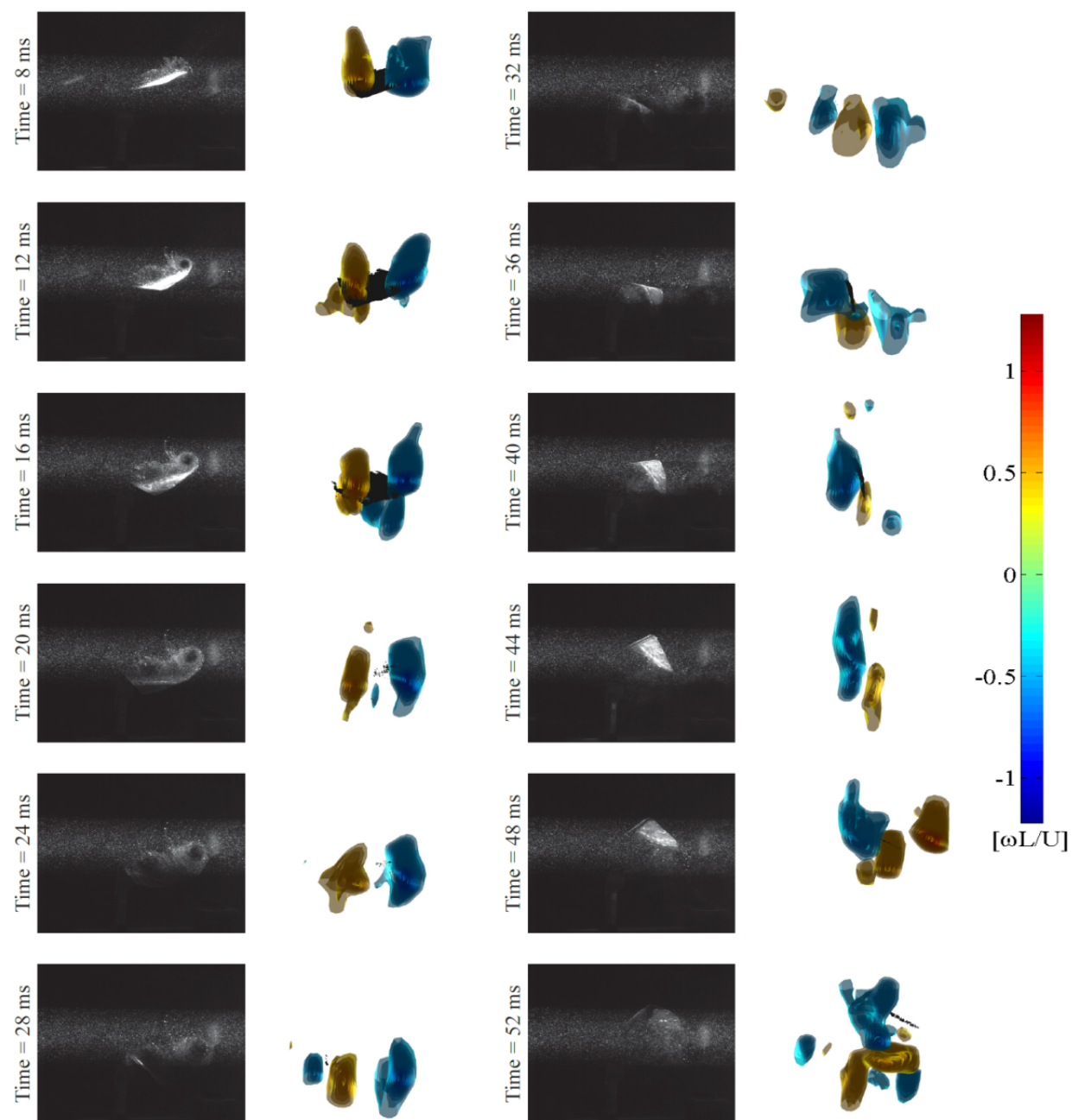
The LEV and TEV remain attached to the wing through the entire down-stroke and up-stroke. The vortices are shed into the wake during the transitions between the up and down strokes. This is evident at time 28 ms when the wing is transitioning from down-stroke to up-stroke. The LEV from the down-stroke on the bottom side of the wing (center structure) is seen leaving the leading edge and moving into the wake as a new LEV (left structure) is seen forming on the leading edge on the top side of the wing. During the down-stroke, the LEV and TEV form and remain attached to the top of the wing, and likewise during the up-stroke, the LEV and TEV form and remain attached to the bottom of the wing. A top view of the wing shows the varying shape of the LEVs and TEVs along the span of the wing (Fig. 10). A look at the cross section shows that, at mid-span of the wings, the LEV has a minimum diameter. The LEV shows greater size at the wing tip.

Figure 9 shows vorticity slices from the 3D velocity fields at 65% of the half span, as well as the vorticity plots from the 2D PIV at 60% half-span, at 14 time steps from mid-down-stroke through an entire flapping period (8 ms to 60 ms). The comparison is promising, showing agreement in the formation and behavior of the LEV and TEV on the MAV wing. In both cases, the LEV is seen to remain attached to the leading edge of the wing throughout the down-stroke. The growth of the LEV can also be seen through the four time steps shown of the down-stroke. In the last frame the wing enters the transition between down-stroke and up-stroke. The shedding of the TEV is visible and the beginning of the shedding of the LEV is also visible.

Differences are seen in the flow beneath the wing. In the 2D PIV plots, vortices are seen under the wing that are not visible in the SAPIV slices. This is due to the 2D PIV plots being shown after a previous flapping period while the SAPIV slices are from the first flapping period. The vortices in the 2D PIV plots are the shed LEV and TEV from the up-stroke previous to the down-stroke shown in the plots. It appears that the vortical structures from the previous stroke are partially recaptured in the current stroke instead of being entirely shed into the wake.

The vortical structures in the 3D PIV plots are more apparent in the down-stroke than the up-stroke. This is due to the turbulence introduced inside the acrylic observation tank as the MAV wings move the air around. The up-stroke comes after the initial down-stroke in the experiment; thus, the LEV and TEV in the up-stroke are less distinguishable than in the down-stroke.





**Figure 7.** Iso-surfaces of vorticity about the z-axis plotted for 12 time steps covering 0.75 wing beats. A down-stroke persists from 1 ms to 21 ms. 50% of the up-stroke is shown from 25 ms to 45 ms.



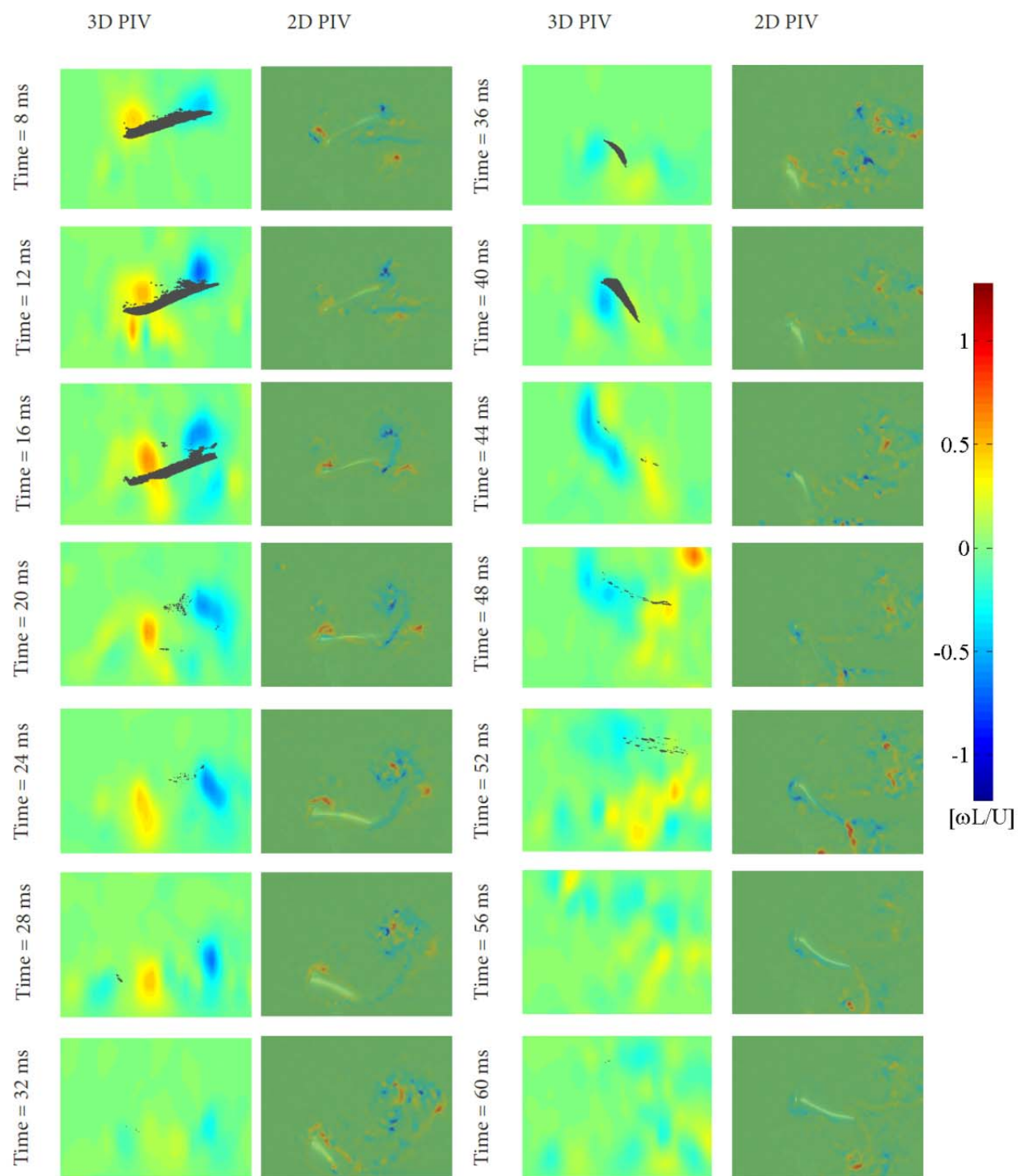


**Figure 8.** A comparison of the SAPIV (left columns) and 2DPIV (right columns) data with the applying period shown in 14 time steps.

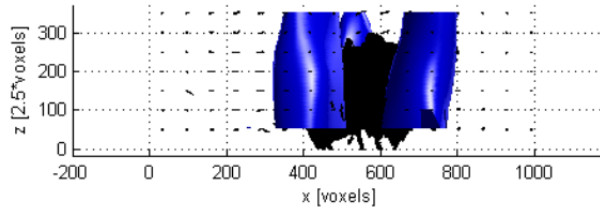


**Figure 9.** Top view of the wing at mid-down-stroke. The diameter of the LEV (left) and TEV (right) vary from the wing mid span (top) to the wing tip (bottom).

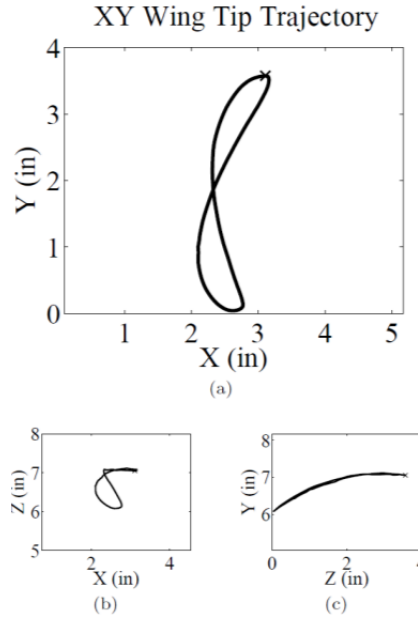
The visual hull of the wing represents the volume in which the wing is contained, but requires large connected components for the algorithm to process. The reconstruction of the wing could be improved by less particle seeding or by adding more light sources so that the intensity of the wing is the same in all camera views to assist in connected component identification. In the results presented in Fig. 7, the MAV starts with its wing at an angle of about  $45^\circ$  to the  $z$ -axis but as the flight progresses the wing reaches an angle of about  $-45^\circ$  with respect to the  $z$ -axis. By using multiple cameras, particles that are obscured in one camera view are visible in other camera views, thus providing whole-field measurements at each wing position. The 2D PIV vorticity plots show greater detail in the LEV and TEV. Despite the lower resolution in the 3D SAPIV data, it is possible to see similarities in the structure and behavior of the vortices. Greater resolution for the SAPIV results can be attained by reducing the size of the volume of interest. This will make it more difficult to visualize the entire flapping period in one experimental run, but would provide greater detail for selected phases of the flapping period.

The wing position was determined by tracking the wing tip of the MAV and plotting the pixel locations. It was observed that the MAV has an interesting wing tip trajectory in the  $x$ - $y$  plane (Fig. 10a). The wing is driven by an electric motor through a four-bar linkage, providing an up and down motion. However, the wing tip follows a skewed figure-eight trajectory, with the figure-eight skewed in the forward direction.

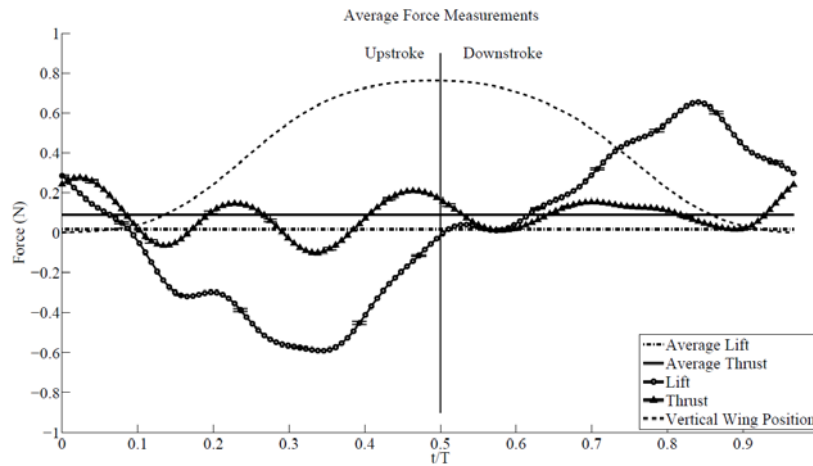
A further investigation of the wing tip trajectory was performed by including a second SA3 camera in the acquisition loop and performing a direct linear transform (DLT) analysis of the wing tip position. The trajectory of the wing tip in the  $x$ - $y$ ,  $x$ - $z$ , and  $y$ - $z$  planes can be seen in Fig. 10. The skewed figure-eight trajectory is seen in the  $x$ - $y$  plane (Fig. 10a), and the wing trajectory has a curvature with a radius equal to the span-wise length of the wing (Fig. 10c). The trajectory in the  $x$ - $z$  plane (Fig. 10b) appears to deviate from the symmetric trajectory pattern as in the other planes; however, it can be seen in Fig. 10c that the wing is not flapping symmetrically with the  $x$ ,  $y$ , and  $z$  axes chosen. However, the same symmetry is exhibited along an axis skewed from the chosen axes.

Figure 11 shows the mean lift and thrust forces generated from 55 flapping periods. The force data was processed using a 3<sup>rd</sup>-order, 120 Hz low-pass Butterworth filter to remove a 150 Hz signal present in both the lift and thrust force measurements generated by the motor and gearing of the four-bar linkage driving the wings. The plot is split down the center to distinguish the up-stroke from the down-stroke of the flapping period.

In the up-stroke, the lift force is negative, with a minimum near the end of the up-stroke occurring at  $-0.58$  N. The primary generation of the negative lift force is the downward force generated by the upward movement of the wing. There is also negative lift generated by the LEV witnessed on the underside of the wing during the up-stroke. During the down-stroke, the forces are reversed; an upward force is generated by the downward movement of the wing, and positive lift is generated. The maximum lift force occurs during the second half of the down-stroke at  $0.6405$  N. The lift is generated by the LEV present on top of the wing during the down-stroke.



**Figure 10.** 3-dimensional trajectory of the wing tip as determined by performing a DLT analysis. The trajectory is plotted on the XY (a), XZ (b), and Y Z (c) planes.



**Figure 11.** Lift and thrust measurements taken using a single-axis load cell. The plots represent the forces seen over one flapping period, averaged over 55 flapping periods. Error bars are plotted for the lift and thrust measurements.

The weight of the MAV was 0.1275 N (calculated using the load cell). By taking the average force over the entire flapping period, the net lift and net thrust (less the weight of the MAV) were determined to be 0.014 N and 0.084 N, respectively, with 95% confidence. This translates to a net lift force 11.0% greater than the weight of the MAV and a net thrust force 65.9% greater than the weight of the MAV.

The vortical structures on the MAV were observed using both SAPIV and 2DPIV. Changing cross sections of the LEV and TEV show evidence of spanwise flow in the direction of the wing tip. The 3D vorticity plots and 2D slice vorticity plots show the three-dimensional nature of the LEV and TEV. And finally, the 2DPIV plots and the 2D slices from the 3D data show general agreement in the structure and behavior of the flow around the flapping wing. Further work can be done to study the expected span wise flow using smaller search volumes and larger experimental volumes to reduce air circulation within

the acrylic box.

Multiple viewpoints used in SAPIV allow for the ability to see around partial occlusions, including high seeding densities. SAPIV is able to reconstruct 3D whole-field velocity fields in large spatial regions of interest and the whole-field nature of the velocity fields allows for analysis of flow characteristics not rectified with the camera axes. The results demonstrate that SAPIV can be used to measure fluid flow velocities and reconstruct the visual hull of flapping wings, with anticipated application in studying the complex and unsteady nature of this flight regime.

## REFERENCES

1. George, R., Colton, M., Mattson, C., and Thomson, S., 2012. "A differentially driven flapping wing mechanism for force analysis and trajectory optimization." *International Journal of Micro Air Vehicles*, 4(1), pp. 31–49.
2. George, R. B., 2011. "Design and analysis of a flapping wing mechanism for optimization." Master's thesis, Brigham Young University, August.
3. Naegle, N. S., 2012. "Force optimization and flow field characterization from a flapping wing mechanism." Master's thesis, Brigham Young University, December.
4. Wilcox, M. Thesis in progress, Brigham Young University, Expected completion Dec. 2013.
5. Duffield, M. L., Mattson, C. A., and Colton, M., 2012. "Towards variable fidelity optimization with hardware in the loop for flapping flight." 14th AIAA/ISSMO Multidisciplinary Analysis and Optimization Conference, Indianapolis, Indiana, AIAA Paper 2012-5692, Sep. 17-19, 2012.
6. Duffield, M. L. "Variable Fidelity Optimization with Hardware-in-the-Loop for Flapping Flight," Master's Thesis, Brigham Young University, 2012.
7. Langley, K. R., Hardester, E., Thomson, S. L., Truscott, T. T. "Three-dimensional flow measurements on flapping wings using synthetic aperture PIV," to be submitted, *Experiments in Fluids*.